

# Numerical field calculations considering the human subject for engineering and safety assurance in MRI

Christopher M. Collins<sup>a\*</sup>

Numerical calculations of static, switched, and radiofrequency (RF) electromagnetic (EM) fields considering the geometry and EM properties of the human body are used increasingly in MRI to explain observed phenomena, explore the limitations of various approaches, engineer improved techniques and technology, and assure safety. As the static field strengths and RF field frequencies in MRI have increased in recent years, the value of these methods has become more pronounced and their use has become more widespread. With the recent growth in parallel reception techniques and the advent of transmit RF arrays, the utility of these calculations will become only more critical to continued progress of MRI. Proper relation of field calculation results to the MRI experiment can require significant understanding of MRI physics, EM field principles, MRI coil hardware, and EM field safety. Here some fundamental principles are reviewed and current approaches and applications are catalogued to aid the reader in finding resources valuable in beginning field calculations for their own applications in MR, with an eye to the current needs and future utility of numerical field calculations in MRI. Copyright © 2008 John Wiley & Sons, Ltd.

**Keywords:** MRI; simulations; specific energy absorption rate; signal-to-noise ratio;  $B_1$ ;  $B_0$ ; gradient

## INTRODUCTION

In the form used most commonly for medical purposes, MRI requires application of three different types of magnetic fields to the subject being imaged: a static magnetic ( $B_0$ ) field to align nuclear magnetic moments, radiofrequency (RF) magnetic ( $B_1$ ) fields to re-orient the net nuclear magnetization and detect a signal, and linear magnetic field gradients that are switched on and off rapidly during the imaging process to encode information about spatial location into the frequency and phase of the signal detected.

All three of these fields interact with the human body in different ways. Interactions can cause both desirable and undesirable effects in the final images produced. For example, slight perturbations in  $B_0$  caused by minute differences in the magnetic permeability ( $\mu_r$ ) between oxygenated and deoxygenated blood can contribute to our ability to detect localized brain function with MRI. Slightly larger perturbations of  $B_0$  near air/tissue interfaces, and much larger perturbations of  $B_1$  (related to tissue relative electrical permittivity,  $\epsilon_r$ , and tissue electrical conductivity,  $\sigma$ ) can, however, lead to severe image distortions and loss of signal.

Besides affecting the images, interactions between the electromagnetic (EM) fields in MRI and human tissues can have implications for patient safety and comfort. RF fields can induce heating of tissues, and time-varying fields – such as the switched gradient fields or motion within a static magnetic field – can result in stimulation of sensory or motor neurons.

Numerical calculations have been used to study the behavior of the EM fields within the human body in MRI for improved understanding of their effects on images and for assurance of patient safety and comfort. This paper is largely a review of methods used to perform these calculations and to evaluate the results. Because it is not possible to review this very broad area in its entirety in a single article, here emphasis is placed on work that considers complex sample geometries, work yielding

important insights, work of particular significance, and work dealing with the current cutting edge of MR technology.

## NUMERICAL CALCULATIONS OF $B_0$ FIELDS

The difference in  $\mu_r$  between different tissues or between human tissues and air is exceedingly small – on the order of a few parts per million. Owing to the nature of MRI, however, this can be enough to cause very severe distortions and signal loss in some types of images. A number of authors have used a variety of methods to calculate  $B_0$  fields in the human body for different purposes (1–10). Most of these studies were geared toward evaluating field perturbations with the goal of understanding and/or correcting image distortions. At least two of them were aimed at evaluating peripheral nerve stimulation or other potential biological effects due to motion in a static magnetic field (5,10).

The majority of the aforementioned studies present the numerically calculated  $B_0$  fields and compare them with analytical calculations and/or experimental measurement, discussing the accuracy and speed of the calculation method. In general, the more recent methods are very fast and accurate and lend themselves well to three-dimensional models on a regular

\* Correspondence to: C. M. Collins, NMR/MRI Bldg, H066, 500 University Drive, Hershey, PA 17033, USA.  
E-mail: cmcollins@psu.edu

a C. M. Collins  
Department of Radiology, The Pennsylvania State University, Hershey, PA 17033-0850, USA  
Contract/grant sponsor: NIH; contract/grant number: R01 EB000454, R01 EB000895, R01 RR16105, and R21 EB001519.

**Abbreviations used:** EM, electromagnetic; RF, radiofrequency; SAR, specific energy absorption rate; SI, signal intensity; SNR, signal-to-noise ratio.

grid, such as those segmented from an MR or computed tomography dataset. Other previous works have also taken the results of analytical field calculations and used them to predict the appearance of MR images of samples with simple geometries (11,12).

## NUMERICAL CALCULATION OF SWITCHED GRADIENT FIELDS

The presence of the human body does not perturb the switched gradient magnetic fields used in MRI enough to notably affect the resulting images. The switched magnetic fields can, however, induce electric fields and currents strong enough to cause peripheral nerve stimulation (PNS) resulting in either a tactile sensation (feeling similar to being touched, pinched, or poked) or a muscle contraction at some frequency corresponding to the switching of the fields. Generally, these nerve stimulations occur at the periphery of the body, and there has been little warranted concern in recent years of any long-term adverse effects (such as could potentially be caused by cardiac stimulation) as long as the gradient fields are not switched at a rate and strength that induces severe discomfort or painful nerve stimulation at the periphery (13). A number of authors have used a variety of methods to calculate gradient-induced fields in the human body to either gain a better understanding of the relationship between gradient fields and PNS or engineer coil designs that may be able to achieve a higher rate of switching without inducing PNS (14–20).

On the whole, these methods have shown success in comparison with analytical field calculations, but results are mixed when their ability to accurately predict locations and levels of PNS are assessed. For example, although there may be high magnetically induced electric fields near the surface of the body in areas where stimulation is known to occur, there are often higher magnetically induced electric fields deep within the body at interfaces between dissimilar tissues, in areas where no stimulation is typically seen. This has raised questions about the mechanism of the neuronal stimulation (14,19) and about the conditions for stimulation (21). The relationship between the electrical fields of the gradient coil induced in the human body and PNS requires further investigation and interpretation and improved understanding.

## NUMERICAL CALCULATION OF RF ELECTROMAGNETIC FIELDS

The vast majority of numerical field calculations performed for MRI of the human subject are related to the RF fields. Whereas perturbations in the static and gradient magnetic fields due to the presence of the human body are only a few parts per million (on the order of 0.000001 times the applied field), perturbations in the  $B_1$  field can easily be tens of a percentage (on the order of 0.1 times the applied field in free space). Also, RF heating in tissue (concomitant with the maintenance of the  $B_1$  field in a lossy medium) must be understood and monitored to avoid excess heating of the subject.

### Numerous field calculation methods

A number of important studies using a variety of methods have led to great insights into behavior, effects, and safety of RF fields

in MRI. It is important to point out that many key developments and observations have used both analytical and numerical calculations of RF field distributions, power dissipation, and MR signal intensity in simple shapes (22–39), and that these RF field calculations in simple shapes continue to be very useful (40–45), although they have limitations in application to the human body. For example, maximum levels of localized heating in simple shapes tend to be much lower than in anatomical models (46), and axis-symmetric objects (such as spheres and cylinders) are apparently not as amenable to RF shimming as are human anatomies (47). Also, although they have led to important insights in the past, quasi-static approximations (22–25) should be used cautiously, and probably not used much at all above 64 MHz for cases involving the human body. Before three-dimensional anatomical models and calculation methods were accessible, some researchers approximated parts of the human body as infinitely long extrusions of a single cross-section (48–50). Although this sometimes led to important insights, infinitely long geometries and excitations lead to exaggerated estimates of RF field distortions and heating (35). In recent years, numerous authors have developed detailed three-dimensional models of the human head (46,51–57) and body (58–60) for use in MRI. Because in many cases a carefully tuned coil (or model) will have a current distribution much like that expected ideally for its resonant condition (60), in many circumstances accurate results can be produced from calculations with assigned current or voltage distributions in the coil (61,41). In other cases, tuning the coil model to the desired frequency and driving it as in experiments (62–70) may be preferable. Whatever method is used, it is important to understand its strengths, limitations, and appropriateness for the specific application (71). Methods for tuning the coil model include iteratively changing capacitor values (62–69) between method-specific frequency sweeps [including Fourier transform of the time-domain impulse response commonly used in the finite difference time domain (FDTD)] and determination of the required capacitance from input impedance at each gap while driving with the desired current pattern (70,60).

Although the calculation methods in the above studies include (among others) the FDTD method, method of moments, finite element methods, and analytical calculations, FDTD and related methods remain dominant in numerical field calculations that consider realistic human body models. However, it is not the ideal method in all situations, such as when dealing with fields near highly conductive surfaces in any arbitrary orientation, as with most RF coils. Generally, FDTD and related methods rely on a Cartesian grid (with regular or irregular grid spacing), so surfaces at oblique angles are represented in a 'staircase' fashion. Although there are some algorithms to help reduce the shortcomings of FDTD-type methods in these situations (56), other approaches include development (in progress) of human body models for finite element methods (72) and hybrid approaches using one numerical method in regions containing the RF coils, and another in the region containing the human body (73).

### Signal and noise for single-channel coils

Because both the excitation of the nuclear magnetization and the reception of signal intensity rely on interactions between magnetic fields and precessing nuclei, it is necessary to calculate the circularly polarized components of the RF magnetic fields

produced by the RF coils (or antennas) to relate results to MRI. In the case of a single-channel coil, the circularly polarized components,  $\hat{B}_1^+$  and  $\hat{B}_1^-$ , can be calculated as (74)

$$\hat{B}_1^+ = (\hat{B}_x + i\hat{B}_y) \div 2 \quad (1)$$

and

$$\hat{B}_1^- = (\hat{B}_x - i\hat{B}_y)^* \div 2 \quad (2)$$

where  $\hat{B}_1^+$ ,  $\hat{B}_1^-$ ,  $\hat{B}_x$ , and  $\hat{B}_y$  are complex values as denoted with a circumflex,  $i$  is the imaginary unit, the asterisk indicates the complex conjugate, and 'imaginary' components are simply 90° out of phase with 'real' components at the frequency of interest. In practice, with the time-domain methods and a sinusoidal excitation (for either a tuned coil or assumed current distributions),  $\hat{B}_x$  and  $\hat{B}_y$  can be constructed with magnetic field values recorded at two different times 90° out of phase with each other at the frequency of interest (55). With this method, the value recorded at the earlier time point becomes the imaginary component, and the value recorded at the later time point becomes the real component. Whether it is  $\hat{B}_1^+$  or  $\hat{B}_1^-$  that rotates in the direction of nuclear precession and thus induces the flip angle depends on whether the  $B_0$  field is oriented with or against the z-axis. Conventionally, it is assumed that  $\hat{B}_1^+$  rotates in the direction of nuclear precession and is thus the flip-inducing component (74,75), although it should be noted that, with conventional definitions of axis orientations and direction of nuclear spin (in a classical sense), this would require  $B_0$  to be oriented in the negative z direction (76,77).

Although the nuclei precess in only one direction, calculation of a coil's receptivity distribution requires consideration of the circularly polarized component of the magnetic field that rotates in the direction opposite nuclear precession that is created when driving the receive coil (41). This can be explained by considering the field produced when applying the principle of reciprocity to a quadrature coil by driving through the receive side of a quadrature splitter/combiner (26) or from considering interaction of the precessing nuclei with the coil in the laboratory frame (74). So the nuclear excitation (and available signal strength) is by convention related to  $\hat{B}_1^+$  produced by the excitation coil, and received signal is related to  $\hat{B}_1^-$  produced by the receive coil. Thus, for a gradient-echo experiment with a rectangular RF pulse, a long  $TR$  and a short  $TE$  (neglecting effects including those of  $T_1$  and  $T_2$ ), signal intensity (SI) is proportional to the product of  $\sin(\gamma\tau|\hat{B}_1^+|)$  and  $|\hat{B}_1^-|$ . Here  $\gamma$  represents the gyromagnetic ratio (42.58 MHz/T for  $^1\text{H}$ ), and  $\tau$  represents the pulse duration for the RF excitation pulse. More generally,

$$SI \propto f_L^2 \sin(\alpha) |\hat{B}_1^-| \quad (3)$$

where  $\alpha$  represents the flip angle, which is a function of the applied  $\hat{B}_1^+$  and its interaction with the net nuclear magnetization vector through space and time, and  $f_L$  is the frequency of nuclear precession (equal to the  $B_1$  field frequency and proportional to the  $B_0$  field strength). SI is proportional to  $f_L$  once because the number of nuclei aligned with  $B_0$  at equilibrium increases with the strength of  $B_0$ , and a second time because the signal induced in the coil by the precessing nuclei will be proportional to the precessional frequency, according to Faraday's Law.

Noise is created by random motion of particles, including (but not limited to) translational motion of electrons in the coil, translational motion of ions in the sample, and rotational motion of dipolar molecules in the sample. These random motions result

in random currents in the receive coil and random voltages at its terminals. It can be shown that the noise detected from these random motions is closely related to the effective resistance of the noise source (78). The noise power induced in the coil by random currents in the sample is proportional to the 'sensitivity' of the coil to these random currents, which, by reciprocity, is proportional to the resistive losses induced in the sample when driving the receive coil. In MRI, we typically calculate the noise as being proportional to the square root of the power dissipated in the coil and/or sample when driving the receive coil with a certain current or voltage. Treating the coil and sample as two resistors in series, the noise voltage can be estimated as:

$$N \propto \sqrt{\alpha P_{coil} + \beta P_{sample}} \quad (4)$$

where  $\alpha$  and  $\beta$  may be different from each other depending on factors such as the absolute temperature of the coil and sample, and  $P_{coil}$  and  $P_{sample}$  are the power dissipated in the coil and sample when driving the receive coil with a certain current or voltage. Generally, this should be the same current or voltage used as when calculating  $\hat{B}_1^-$ .

A general equation relating the signal-to-noise ratio (SNR) to the RF EM fields can be obtained by dividing eqn (3) by eqn (4). For imaging of the human body with relatively large receive coils and at high frequencies, it is generally accepted that  $P_{coil}$  is negligible compared with  $P_{sample}$ . However, as coils in receive arrays become more numerous and smaller, it may be necessary to consider  $P_{coil}$  as well as  $P_{sample}$ . Note that this method of calculating 'intrinsic' SNR (24) neglects numerous real-world factors including dependence of  $T_1$  on  $B_0$ , physiological noise, and imaging parameters. The numerical values are therefore valuable for a variety of purposes including comparing different coil designs and exploring trends with field strength, but they should not be expected to match experimentally measured values.

### Consideration of quadrature coils

A circularly polarized magnetic field can be created with the superposition of two orthogonal linear magnetic fields driven with a 90° phase shift between them. Most transmit coils and many receive coils used today are quadrature coils – designed to take advantage of this principle to produce more efficient excitation (requiring less power to be applied and absorbed into the subject) and/or higher SNR. Popular coils that are particularly suited to quadrature use are the birdcage coil (79) and the TEM resonator (49).

For a transmit/receive coil used in quadrature, it is necessary to calculate the pertinent  $\hat{B}_1^+$  and  $\hat{B}_1^-$  fields as if they were produced from different driving configurations: the first with the driving voltages designed to create a field rotating in the same direction as nuclear precession, and the second with driving voltages designed to create a field rotating opposite nuclear precession (26,74). In other words, to calculate the excitation distribution,  $\hat{B}_1^+$ , it is necessary to simulate the fields produced when driving the coil through the transmit side of the quadrature splitter/combiner, and to calculate the receptivity distribution,  $\hat{B}_1^-$ , it is necessary to simulate the fields produced when driving the coil through the receive side of the quadrature splitter/combiner. In the case of the human head in quadrature volume coils (such as birdcage or TEM coils) at frequencies from 128 to 400 MHz, the result is that both the  $\hat{B}_1^+$  and  $\hat{B}_1^-$  distributions will be stronger at the center (where primarily constructive interference occurs)

than in a surrounding region (where destructive interference weakens the field). The destructive interference has its maximum adverse effect roughly one-quarter wavelength away from the center (32,43,80).

### Receive arrays

Often the signal received from multiple coils is combined in creative ways to improve SNR (81) or reduce acquisition time (82–85). A number of very diverse methods are used to accomplish these aims, and their implementation can be fairly involved. It is thus beyond the scope of this work to discuss this topic in detail, but calculations of EM fields of the receive coils can be used to predict SI distribution and/or SNR distribution for these methods (42,83). One effect of some receive-array reconstruction methods is to reduce the impact of the  $\hat{B}_1^-$  distribution on the SI distribution of the final image (81,83,86), but compared with the single-coil case described above, the SNR distribution becomes quite complicated, being a function of the overlapping magnetic and electric fields of the receive coils, the  $k$ -space trajectory, and the image reconstruction algorithm.

### Transmit arrays

A very recent development in MRI is the use of multiple simultaneous transmit coils, or a transmit array. Field calculations are currently used extensively in the exploration of methods to use this technology to shorten pulse durations, create homogeneous excitations, and reduce heating of the subject (40,45,56,73,76,87–102). Although other methods have been proposed (87,89), the two most popular approaches at this time can be categorized as RF shimming and multi-coil tailored pulses.

RF shimming typically involves merely adjusting the magnitude and phase of the currents in the elements of the transmit array to produce a desired RF field distribution in the region of interest, usually without any explicit consideration of the nuclear magnetization vectors throughout space and time (40,56,73,76,88,90,94,95,97,99). RF shimming techniques have also been simulated with the purpose of achieving localized excitation (87,88,94), but they do not have nearly as precise control in this area as multi-coil tailored pulses. Recent simulations of RF shimming methods that attempt to achieve both improved magnetic field homogeneity and reduced subject heating also show great promise (90,94,95).

Multi-coil tailored pulses, including Transmit SENSE (103), have greater technical requirements than RF shimming, but also have tremendous flexibility in terms of the pattern of excitation produced (45,91–93,101,102). These methods generally require highly specialized RF pulses (different in each coil) driven simultaneously with gradient pulses to achieve a pre-determined spatially selective excitation pattern while traversing a pre-determined trajectory through  $k$ -space. They are designed to achieve rotation of the nuclear magnetization vectors in a specified pattern throughout space. The RF and gradient field distributions through time are tools to achieve this, but the RF field distribution itself is not adjusted to match a target as in RF shimming. With the use of multiple coils, it is possible to achieve much shorter pulse durations than with the use of a single coil, and it is expected that this may also reduce the specific energy absorption rate (SAR) relative to that achievable with a single coil (103). Methods that simultaneously produce the desired excitation distributions and reduce SAR using multi-coil tailored

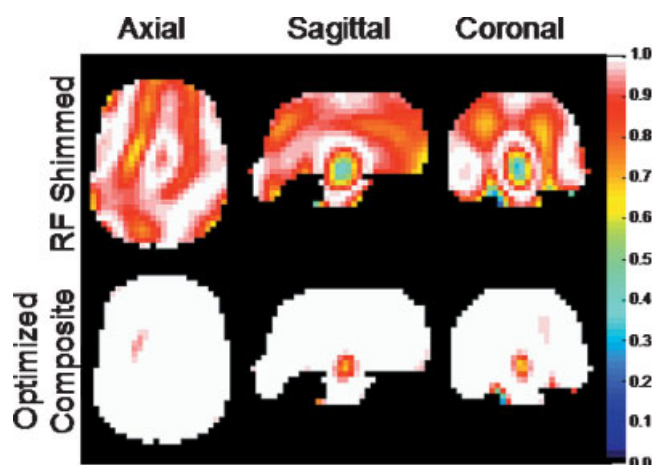


**Figure 1.** Sine of flip angle of nuclear magnetization vector after RF shimming (top) and an array-optimized composite pulse (bottom) optimized over the entire brain in a complete human head model at 600 MHz in a 16-element transmit array. The composite pulse consisted of two short consecutive pulses with different RF field distributions.

pulses have also been explored recently using numerical field calculations (92,93,101,102).

Although RF shimming is sufficient to produce remarkably homogeneous images on single planes through the head at very high frequencies (40,76,104), its limitations in the body and over large volumes have caused investigators to limit it to only certain regions in a plane at a time in high-field MRI of the body (88,105). Multi-coil tailored pulses, on the other hand, are very flexible in the variety of spatial excitation distributions that they can achieve throughout the human body. Other methods may also have advantages and warrant further investigation. As an example, a series of short RF pulses with minimal time between, and with RF field distributions varied between pulses to produce a homogeneous nuclear excitation, shows a dramatic advantage over RF shimming alone, but requires less complicated pulse design than multi-coil tailored pulses (89,100). Available SI for gradient echo imaging in the human head at 14 T is shown in Fig. 1 for cases where the whole brain volume was excited with RF shimming and with an array-optimized composite pulse consisting of only two short pulses. Theory and methods are described in much greater detail elsewhere (89).

### RF power absorption

Besides its relationship to noise (discussed above), power absorbed by the human subject during RF excitation causes heating of the tissue. SAR (units of W/kg) is the entity most often discussed in terms of monitoring and regulating the heating of tissues. In MRI, there are regulations for SAR over the whole body, over the head, over any portion of the body, and the maximum SAR averaged over any 10 g region of the body (106). The regulations are applicable to SAR averaged over periods of from 10 s to 6 min, so SAR can generally be reduced by reducing the energy absorbed during the pulses or by increasing the repetition time,  $TR$ , in the experiment. Some researchers have published work relating calculations of SAR specifically to the regulatory limits for MRI (46,55,59,60,97,107–113).

Recognizing that it is not power absorption alone, but temperature, that can cause damage, some authors have used the results of SAR calculations and calculated the resulting

temperature increase (108,111–115). Because temperature is affected by many factors besides SAR (most notably blood perfusion rate and thermal conductivity), the correlation between SAR patterns and heating patterns is often not good. Challenges in this area include finding recent, accurately measured values for blood perfusion rates of different tissues. In other fields, such as radiation therapy, much emphasis is placed on accurate modeling of blood vessel geometry because the presence of blood vessels has a cooling effect on adjacent tissue which can result in lower than desired heating in those applications. In calculations for MRI, ignoring this cooling effect should only result in more conservative estimates for purposes of ensuring safety.

The development of transmit array capability presents a particular challenge for safety assurance and a valuable opportunity for use of numerical methods. Unlike conventional excitation methods, a transmit array can be driven with a different current distribution for different subjects, or even at different times in one pulse, as with multi-coil tailored pulses. Although it should still be possible to monitor average SAR levels as has been done for decades (by estimating the total power absorbed in the subject and dividing that by the mass of the exposed region), to assure that local SAR levels do not reach excessive levels will require development of new methods. One approach is to use superposition of previously calculated results to estimate local SAR levels in real time during an experiment. Under the right circumstances, this could be accomplished rapidly and accurately enough to ensure safety without causing any delay in the study (116). Considering potential effects of any failures in the drive chain to the coils, it may also be desirable to directly monitor the fields produced by each element (98).

A significant challenge for RF safety assurance is the dependence of local SAR levels on individual patient anatomy (60). All currently available anatomically accurate numerical body models are based on information from only a handful of individuals, and thus are not representative of the wide anatomical variation among actual human subjects. For field calculations to be able to contribute more significantly to safety assurance, it will be necessary to develop and disseminate models of a much wider variety of human subject anatomies.

## CONCLUSION

In MRI, numerical field calculations are used for numerous purposes and are increasingly valuable. With careful preparation and analysis, numerical calculations can be used to engineer improvements in MR technology, explore the limits of what is possible with current technology, explain observed phenomena, and ensure patient safety. Although many important topics have only been briefly reviewed here, it is hoped that, in combination with the extensive list of references (as well as the discussion and further references therein), this work will be a valuable resource for those seeking to perform field calculations for their own applications within MRI.

## REFERENCES

1. Bhagwandien R, Moerland MA, Bakker CJG, Beersma R, Lagenijk JJW. Numerical analysis of the magnetic field for arbitrary magnetic susceptibility distributions in 3D. *Magn. Reson. Imag.* 1994; 12: 101–107.
2. Li S, Dardzinski BJ, Collins CM, Yang QX, Smith MB. Three-dimensional mapping of the static magnetic field inside the human head. *Magn. Reson. Med.* 1999; 36: 705–714.
3. Collins CM, Yang B, Yang QX, Smith MB. Numerical calculations of the static magnetic field in three-dimensional multi-tissue models of the human head. *Magn. Reson. Imaging* 2002; 20: 413–424.
4. Truong TK, Clymer BD, Chakeres DW, Schmalbrock P. Three-dimensional numerical simulations of susceptibility-induced magnetic field inhomogeneities in the human head. *Magn. Reson. Imaging* 2002; 20: 759–770.
5. Liu F, Zhao HW, Crozier S. Calculation of electric fields induced by body and head motion in high-field MRI. *J. Magn. Reson.* 2003; 161: 99–107.
6. Salomir R, De Senneville BD, Moonen CTW. A fast calculation method for magnetic field inhomogeneity due to an arbitrary distribution of bulk susceptibility. *Concepts in Magnetic Resonance Engineering Part B – Magnetic Resonance Engineering* 2003; 19B: 26–34.
7. Jenkinson M, Wilson JL, Jezzard P. Perturbation method for magnetic field calculations of nonconductive objects. *Magn. Reson. Med.* 2004; 52: 471–477.
8. Marques JP, Bowtell R. Application of a fourier-based method for rapid calculation of field inhomogeneity due to spatial variation of magnetic susceptibility. *Concepts in Magnetic Resonance Engineering Part B – Magnetic Resonance Engineering* 2005; 25B: 65–78.
9. Koch KM, Papademetris X, Rothman DL, de Graaf RA. Rapid calculations of susceptibility-induced magnetostatic field perturbations for *in vivo* magnetic resonance. *Phys. Med. Biol.* 2006; 51: 6381–6402.
10. Crozier S, Trakic A, Wang H, Liu F. Numerical study of currents in occupational workers induced by body-motion around high-ultrahigh field MRI magnets. In *Proceedings of the Joint Annual Meeting ISMRM-ESMRMB*, May 19–25, 2007, Berlin, p. 1098.
11. Ludeke KM, Roschmann P, Tischler R. Susceptibility artefacts in NMR imaging. *Magn. Reson. Imag.* 1985; 3: 329–343.
12. Benoit-Cattin H, Collwet G, Belaroussi, Saint-Jalmes H, Odet C. The SIMRI project: a versatile and interactive MRI simulator. *J. Magn. Reson.* 2005; 173: 97–115.
13. Center for Devices and Radiologic Health. *Criteria for significant risk investigations of magnetic resonance diagnostic devices*. Food and Drug Administration: Rockville, 2003.
14. Forbes LK, Crozier S. On a possible mechanism for peripheral nerve stimulation during magnetic resonance imaging scans. *Phys. Med. Biol.* 2001; 46: 591–608.
15. Brand M, Heid O. Induction of electric fields due to gradient switching: a numerical approach. *Magn. Reson. Med.* 2002; 48: 731–734.
16. Liu F, Zhao W, Crozier S. On the induced electric field gradients in the human body for magnetic stimulation by gradient coils in MRI. *IEEE Trans. Biomed. Eng.* 2003; 50: 804–811.
17. McKinnon G. Simplifying gradient coil modeling in FDTD calculations. In *Proceedings of the 11th Annual Meeting of ISMRM*, Toronto, 2003, p. 2437.
18. Bowtell R, Bencsik M, Bowley R. Reducing peripheral nerve stimulation due to switched transverse field gradients using additional concomitant field coil. In *Proceedings of the 11th Annual Meeting of ISMRM*, Toronto, 2003, p. 2424.
19. Mao W, Chronik BA, Feldman RE, Smith MB, Collins CM. Calculations of the complete electric field within a loaded gradient coil. *Magn. Reson. Med.* 2006; 55: 1424–1432.
20. Crozier S, Wang H, Trakic A, Liu F. Modelling regulatory compliance of occupationally exposed MRI workers during gradient pulsing. In *Proceedings of the Joint Annual Meeting ISMRM-ESMRMB*, May 19–25, 2007, Berlin, p. 1089.
21. Chronik BA, Ramachandran M. Simple anatomical measurements do not correlate significantly to individual peripheral nerve stimulation thresholds as measured in MRI gradient coils. *J. Magn. Reson. Imaging* 2003; 17: 716–721.
22. Bottomley PA, Andrew ER. RF magnetic field penetration, phase shift and power dissipation in biological tissue: implications for NMR imaging. *Phys. Med. Biol.* 1978; 23: 630–643.
23. Hoult DI, Lauterbur PC. The sensitivity of the zeugmatographic experiment involving human samples. *J. Magn. Reson.* 1979; 34: 425–433.
24. Edelstein WA, Glover GH, Hardy CJ, Redington RW. The intrinsic signal-to-noise ratio in NMR imaging. *Magn. Reson. Med.* 1986; 3: 604–618.

25. Bottomley PA, Redington RW, Edelstein WA, Schenck JF. Estimating radiofrequency power deposition in body nmr imaging. *Magn. Reson. Med.* 1985; 2: 336–349.
26. Glover GH, Hayes CE, Pelc NJ, Edelstein WA, Mueller OM, Hart HR, Hardy CJ, O'Donnell M, Barber WD. Comparison of linear and circular polarization for magnetic resonance imaging. *J. Magn. Reson.* 1985; 64: 255–270.
27. Keltner JR, Carlson JW, Roos MS, Wong TS, Wong TL, Budinger TF. Electromagnetic fields of surface coil *in vivo* NMR at high frequencies. *Magn. Reson. Med.* 1991; 22: 467–480.
28. Ochi H, Yamamoto E, Sawaya K, Adachi S. Calculation of electromagnetic field of an MRI antenna loaded by a body. In *Book of Abstracts, 11th Annual Meeting, Society of Magnetic Resonance in Medicine, Berlin, 1992*; p. 4021.
29. Petropoulos LS, Haacke EM, Brown RW, Boerner E. Predicting RF field penetration in heterogeneous bodies using a 3D finite element approach: preliminary results. *Magn. Reson. Med.* 1993; 30: 366–372.
30. McRobbie DW. Radio frequency eddy current losses for an annular conductor in MRI: theory and applications. *Med. Phys.* 1993; 20: 1555–1560.
31. Han Y, Wright SM. Analysis of RF penetration effects in MRI using finite-difference time-domain method. In *Proceeding of the Society for Magnetic Resonance in Medicine, 12<sup>th</sup> Annual Meeting*. 1993; p. 1327.
32. Tofts PS. Standing waves in uniform water phantoms. *J. Magn. Reson.* 1994; 104B: 143–147.
33. Yang QX, Wang JH, Collins CM, Smith MB, Zhang X, Liu H, Michaeli S, Zhu X-H, Adriany G, Vaughan JT, Anderson P, Ugurbil K, Chen W. Analysis of Wave Behavior in Dielectric Samples at High Field. *Magn. Reson. Med.* 2002; 47: 982–989.
34. McDuffie JH, Harrison JG, Pohost GM, Vaughan JT. 3D numerical modeling of high frequency volume coils for clinical NMR. In *Proceedings of the Society of Magnetic Resonance, 3rd Scientific Meeting, Nice, 1995*; p. 185.
35. Collins CM, Li S, Yang QX, Smith MB. Importance of accurate geometry in high-frequency B<sub>1</sub> calculations. In *Proceedings of the ISMRM 4th Scientific Meeting and Exhibition*. 1996; p. 253.
36. Guclu C, Kashmar G, Hacinliyan A, Nalcioglu O. An FEM approach for the characterization of the field homogeneity at high field. *Magn. Reson. Med.* 1997; 37: 76–83.
37. Singerman RW, Denison TJ, Wen H, Balaban RS. Simulation of B<sub>1</sub> field distribution and intrinsic signal-to-noise in cardiac MRI as a function of static magnetic field. *J. Magn. Reson.* 1997; 125: 72–83.
38. Strilka RJ, Li S, Martin JT, Collins CM, Smith MB. A numerical study of radiofrequency deposition in a spherical phantom using surface coils. *Magn. Reson. Imaging* 1998; 16: 787–798.
39. Ocali O, Atalar E. Ultimate intrinsic signal-to-noise ratio in MRI. *Magn. Reson. Imaging* 1998; 39: 462–473.
40. Houtl DI. The sensitivity and power deposition of the high field imaging experiment. *J. Magn. Reson. Imaging* 2000; 12: 46–67.
41. Collins CM, Yang QX, Wang JH, Zhu X-H, Adriany G, Michaeli S, Vaughan JT, Zhang X, Liu H, Anderson P, Ugurbil K, Smith MB, Chen W. Different excitation and reception distributions with a single-loop transmit-receive surface coil near a head-sized spherical phantom at 300 MHz. *Magn. Reson. Med.* 2003; 47: 1026–1028.
42. Wiesinger F, Van de Moortele P-F, Adriany G, De Zanche N, Ugurbil K, Pruessmann KP. Parallel imaging performance as a function of field strength—an experimental investigation using electrodynamic scaling. *Magn. Reson. Med.* 2004; 52: 953–964.
43. Collins CM, Liu W, Schreiber W, Yang QX, Smith MB. Central brightening due to constructive interference with, without, and despite dielectric resonance. *J. Magn. Reson. Imag.* 2005; 21: 192–196.
44. Wang Z, Collins CM, Smith MB. Toward understanding SAR patterns in the human head at high field (200 to 400 MHz) MRI with volume coils. In *14<sup>th</sup> Scientific Meeting and Exhibition of the International Society for Magnetic Resonance in Medicine, May 6–12, Seattle, Washington, 2006*; p. 1390.
45. Lattanzi R, Grant AK, Sodickson DK, Zhu Y. Electrodynamic constraints on minimum SAR in parallel excitation. In *Joint Annual Meeting ISMRM-ESMRMB, May 19–25, Berlin, 2007*; p. 675.
46. Collins CM, Li S, Smith MB. SAR and B<sub>1</sub> field distributions in a heterogeneous human head model within a birdcage coil. *Magn. Reson. Med.* 1998; 40: 847–856.
47. Ibrahim TS. Optimization of RF coils for high field imaging: why the head is different than symmetrical phantoms. In *ISMRM Twelfth Scientific Meeting, May 15–21, Kyoto, 2004*; p. 1643.
48. Smith MB, Ashtiani CN, Cendes ZJ, Williams GD, Martin JT. Finite element calculation of radiofrequency magnetic fields in simulated human organs. In *Book of abstracts, SMRM Eighth Annual Meeting and Exhibition*. 1989; p. 995.
49. Vaughan JT, Hetherington HP, Otu JO, Pan JW, Pohost GM. High frequency volume coils for clinical NMR imaging and spectroscopy. *Magn. Reson. Imaging* 1994; 32: 206–218.
50. Jin J, Chen J. On the SAR and field inhomogeneity of birdcage coils loaded with the human head. *Magn. Reson. Med.* 1997; 38: 953–963.
51. Ko WL. Analyses of RF coils in MRI by FD-TD. In *Annual International Conference of the IEEE Engineering in Medicine and Biology Society* 1991; 13: 85–86.
52. Simunic D, Wach P, Renhart W, Stollberger R. Spatial distribution of high-frequency electromagnetic energy in human head during MRI: numerical results and measurements. *IEEE Trans. Biomed. Eng.* 1996; 43: 88–94.
53. Jin JM, Chen J, Chew WC, Gan H, Magin RL, Dimbylow PJ. Computation of electromagnetic fields for high-frequency magnetic resonance imaging applications. *Phys. Med. Biol.* 1996; 41: 2719–2738.
54. Collins CM, Smith MB. B<sub>1</sub> Field and SAR Distributions in a Heterogeneous Human Head Model. In: *Proceedings of the International Society of Magnetic Resonance in Medicine*. 1998; 6: 442.
55. Collins CM, Smith MB. Signal-to-noise ratio and absorbed power as functions of main magnetic field strength and definition of “90°” RF pulse for the head in the birdcage coil. *Magn. Reson. Med.* 2001; 45: 684–691.
56. Ibrahim TS, Lee R, Baertlein BA, Abduljalil AM, Zhu H, Robitaille PL. Effect of RF coil excitation on field inhomogeneity at ultra high fields: a field optimized TEM resonator. *Magn. Reson. Imaging* 2001; 19: 1339–1347.
57. Angelone LM, Tulloch S, Wiggins G, Iwaki S, Makris N, Bonmassar G. New high resolution head model for accurate electromagnetic field computation. In: *Proceedings of the International Society of Magnetic Resonance in Medicine* 2005; 13: 881.
58. Grandolfo M, Vecchia P, Gandhi OP. Magnetic resonance imaging: calculation of rates of energy absorption by a human-torso model. *Bioelectromagnetics* 1990; 11: 117–28.
59. Collins CM, Smith MB. Calculations of B<sub>1</sub> distribution, SNR, and SAR for a surface coil against an anatomically-accurate human body model. *Magn. Reson. Med.* 2001; 45: 692–699.
60. Liu W, Collins CM, Smith MB. Calculations of B<sub>1</sub> distribution, specific energy absorption rate, and intrinsic signal-to-noise ratio for a body-size birdcage coil loaded with different human subjects at 64 and 128 MHz. *Appl. Magn. Reson.* 2005; 29: 5–18.
61. Alecci M, Collins CM, Wilson J, Liu W, Smith MB, Jezzard P. Theoretical and experimental evaluation of detached endcaps for 3 T birdcage coils. *Magn. Reson. Med.* 2003; 49: 363–370.
62. Han Y, Wright SM. Wide-band RF coil behavior analysis using FDTD method. In *Society for Magnetic Resonance Second Scientific Meeting and Exhibition, San Francisco, 1994*; p. 1133.
63. Ochi H, Yamamoto E, Sawaya K, Adachi S. Calculation of electromagnetic field of an MRI antenna loaded by a body. In *Book of Abstracts, 11th Annual Meeting, Society of Magnetic Resonance in Medicine, Berlin, 1992*; p. 4021.
64. Ochi H, Yamamoto E, Sawaya K, Adachi S. Analysis of MRI antenna inside an RF shield using moment method. In *Proceedings of the Society of Magnetic Resonance in Medicine, 12th Annual Meeting, New York, 1993*; p. 1356.
65. Yang QX, Maramis H, Li S, Smith MB. Three-dimensional full wave solution of MRI radio frequency resonator. In *Proceedings of the Society of Magnetic Resonance, 2nd Annual Meeting, San Francisco, 1994*; p. 1110.
66. Junge S, Haeberlen U. 3D simulations of B and E fields in RF-resonators by CONCEPT and MAFIA. In *Proceedings of the International Society for Magnetic Resonance in Medicine 6<sup>th</sup> Annual Meeting, Sydney, 1998*; p. 2042.
67. Junge S, Haeberlen U. 1999. Optimization of a quadrature whole-body resonator for 2 T. In *Proceedings of the International Society for Magnetic Resonance in Medicine 7<sup>th</sup> Annual Meeting, Philadelphia, 1999*; p. 2053.
68. Ibrahim TS, Lee R, Baertlein BA, Yu Y, Robitaille PML. Computational analysis of the high pass birdcage resonator: finite difference time domain simulations for high-field MRI. *Magn. Reson. Imaging* 2000; 18: 835–843.

69. Vaughan JT, Garwood M, Collins CM, Liu W, DelaBarre L, Adriany G, Andersen P, Merkle H, Goebel R, Smith MB, Ugurbil K. 7 T vs. 4 T: RF power, homogeneity, and signal-to-noise comparison in head images. *Magn. Reson. Med.* 2001; 46: 24–30.
70. McKinnon G, Wang Z. Direct capacitor determination in FDTD modelling of RF coils. In *International Society for Magnetic Resonance in Medicine Eleventh Scientific Meeting and Exhibition*, Toronto, 2003; p. 2381.
71. Collins CM. Radiofrequency field calculations for high field MRI. In *Ultra High Field Magnetic Resonance Imaging*, Robitaille PML, Berliner L (eds). Springer: New York, 2006; 209–233.
72. Vogel MH, Kleihorst RP. Large-scale simulations including a human-body model for MRI. In *IEEE MTT-S 2007 International Microwave Symposium Technical Program*, Honolulu, June 3–8, 2007; p. 1010.
73. Li BK, Liu F, Crozier S. Focused, eight-element transceive phased array coil for parallel magnetic resonance imaging of the chest: theoretical considerations. *Magn. Reson. Med.* 2005; 53: 1251–1257.
74. Hoult DI. The principle of reciprocity in signal strength calculations – a mathematical guide. *Concepts in Magnetic Resonance* 2000; 12: 173–187.
75. Ibrahim TS. Analytical approach to the MR signal. *Magn. Reson. Med.* 2005; 54: 677–682.
76. Collins CM, Liu W, Swift BJ, Smith MB. Combination of optimized transmit arrays and some parallel imaging reconstruction methods can yield homogeneous images at very high frequencies. *Magn. Reson. Med.* 2005; 54: 1327–1332.
77. Haacke EM, Brown RW, Thompson MR, Venkatesan R. *Magnetic Resonance Imaging*. John Wiley & Sons: New York, 1999; p. 29.
78. Nyquist H. Thermal agitation of electric charge in conductors. *Phys. Rev.* 1928; 32: 110–113.
79. Hayes CE, Edelstein WA, Schenck JF, Mueller OM, Eash M. An efficient, highly homogeneous radiofrequency coil for whole-body NMR imaging at 1.5 T. *J. Magn. Reson.* 1985; 63: 622–628.
80. Van de Moortele P-F, Akgun C, Adriany G, Moeller S, Ritter J, Collins CM, Smith MB, Vaughan JT, Ugurbil K. B1 interferences and spatial phase patterns at 7 tesla with a head transceiver array coil. *Magn. Reson. Med.* 2005; 54: 1503–1518.
81. Roemer PB, Edelstein WA, Hayes CE, Souza SP, Mueller OM. The NMR phased array. *Magn. Reson. Med.* 1990; 16: 192–225.
82. Sodickson DK, Manning WJ. Simultaneous acquisition of spatial harmonics (SMASH): ultra-fast imaging with radiofrequency coil arrays. *Magn. Reson. Med.* 1997; 38: 591–603.
83. Pruessmann KP, Weiger M, Scheidegger MB, Boesiger P. SENSE: sensitivity encoding for fast MRI. *Magn. Reson. Med.* 1999; 42: 952–962.
84. Griswold MA, Jakob PM, Nittka M, Goldfarb JW, Haase A. Partially parallel imaging with localized sensitivities (PILS). *Magn. Reson. Med.* 2000; 44: 602–609.
85. Griswold MA, Jakob PM, Heidemann RM, Nittka M, Jellus V, Wang J, Kiefer B, Haase A. Generalized autocalibrating partially parallel acquisitions (GRAPPA). *Magn. Reson. Med.* 2002; 47: 1202–1210.
86. Sodickson DK, McKenzie CA. A generalized approach to parallel magnetic resonance imaging. *Med. Phys.* 2001; 28: 1629–1643.
87. Li BK, Xu B, Liu F, Crozier S. Multiple-acquisition parallel imaging combined with a transceive array for the amelioration of high-field RF distortion: a modeling study. *Concepts Magnetic Resonance Part B – Magnetic Resonance Engineering* 2006; 29B: 95–105.
88. Abraham R, Ibrahim TS. Proposed radiofrequency phased-array excitation scheme for homogenous and localized 7-Tesla whole-body imaging based on full-wave numerical simulations. *Magn. Reson. Med.* 2007; 57: 235–242.
89. Collins CM, Wang Z, Mao W, Fang J, Liu W, Smith MB. Array-optimized composite pulses for excellent whole-brain homogeneity in high field MRI. *Magn. Reson. Med.* 2007; 57: 470–474.
90. Van den Berg CAT, van den Bergen B, Van de Kamer JB, Raaymakers BW, Kroeze H, Bartels LV, Lagendijk JJW. Simultaneous  $B_1^+$  homogenization and specific absorption rate hotspot suppression using a magnetic resonance phased array transmit coil. *Magn. Reson. Med.* 2007; 57: 577–586.
91. Xu D, King KF, Zhu Y, McKinnon GC, Liang Z-P. A noniterative method to design large-tip-angle multidimensional spatially-selective radio frequency pulses for parallel transmission. *Magn. Reson. Med.* 2007; 58: 326–334.
92. Wu X, Akgun C, Vaughan JT, Ugurbil K, Van de Moortele P-F. SAR reduction in transmit SENSE using adapted excitation k-space trajectories. In *Proceedings of the Joint Annual Meeting ISMRM-ESMRMB*, Berlin, May 19–25, 2007; p. 673.
93. Graesslin I, Biederer S, Schweser F, Zimmermann K-H, Katscher U, Börner P. SAR reduction for parallel transmission using VERSE and K-space filtering. In *Proceedings of the Joint Annual Meeting ISMRM-ESMRMB*, Berlin, May 19–25, 2007; p. 674.
94. Ibrahim TS, Tang L. A Whole-body 7 Tesla RF excitation scheme with much improved  $B_1^+$  field homogeneity and local/global SARs over quadrature excitation. In *Proceedings of the Joint Annual Meeting ISMRM-ESMRMB*, Berlin, May 19–25, 2007; p. 1013.
95. Wang Z, Oh S-H, Smith MB, Collins CM. RF shimming considering both excitation homogeneity and SAR. In *Proceedings of the Joint Annual Meeting ISMRM-ESMRMB*, Berlin, May 19–25, 2007; p. 1022.
96. Akgun CE, Snyder CJ, DelaBarre L, Tian J, Van de Moortele P-F, Moeller S, Ugurbil K, Vaughan JT. A novel RF head coil for 7 T homogeneity and parallel imaging applications. In *Proceedings of the Joint Annual Meeting ISMRM-ESMRMB*, Berlin, May 19–25, 2007; p. 1031.
97. McKinnon G. RF shimming and SAR considerations with an eight-element 3 T body coil. In *Proceedings of the Joint Annual Meeting ISMRM-ESMRMB*, Berlin, May 19–25, 2007; p. 1085.
98. Graesslin I, Biederer S, Falaggis K, Vernickel P, Dingemans H, Mens G, Roeschmann P, Leussler C, Zhai Z, Morich M, Katscher U. Real-time SAR monitoring to ensure patient safety for parallel transmission systems. In *Proceedings of the Joint Annual Meeting ISMRM-ESMRMB*, Berlin, May 19–25, 2007; p. 1086.
99. Collins CM, Wang Z, Smith MB. A conservative method for ensuring safety within transmit arrays. In *Proceedings of the Joint Annual Meeting ISMRM-ESMRMB*, Berlin, May 19–25, 2007; p. 1092.
100. Oh S-H, Wang Z, Smith MB, Collins CM. Array-optimized composite pulse for homogeneous whole-brain inversion in high field MRI. In *Proceedings of the Joint Annual Meeting ISMRM-ESMRMB*, Berlin, May 19–25, 2007; p. 1692.
101. Zelinski AC, Setsompop K, Alagappan V, Gagoski BA, Angelone LM, Bonmassar G, Fontius U, Schmitt F, Adalsteinsson E, Wald LL. pulse design methods for reduction of specific absorption rate in parallel RF excitation. In *Proceedings of the Joint Annual Meeting ISMRM-ESMRMB*, Berlin, May 19–25, 2007; p. 1698.
102. Zelinski AC, Goyal VK, Angelone L, Bonmassar B, Wald LL, Adalsteinsson E. Designing RF pulses with optimal specific absorption rate (SAR) characteristics and exploring excitation fidelity, SAR and pulse duration tradeoffs. In *Proceedings of the Joint Annual Meeting ISMRM-ESMRMB*, Berlin, May 19–25, 2007; p. 1699.
103. Katscher U, Börner P, Leussler C, van den Brink JS. Transmit SENSE. *Magn. Reson. Med.* 2003; 49: 144–150.
104. Vaughan JT, DelaBarre L, Snyder C, Tian J, Akgun C, Shrivastava D, Liu W, Olson C, Adriany G, Strupp J, Andersen P, Gopinath A, van de Moortele P-F, Garwood M, Ugurbil K. 9.4 T human MRI: preliminary results. *Magn. Reson. Med.* 2007; 56: 1274–1282.
105. Snyder CJ, DelaBarre L, Van de Moortele P-F, Snyder ALL, Akgun C, Tian J, Metzger G, Ugurbil K, Vaughan JT. Stripline/TEM transceiver array for 7 T body imaging. In *Proceedings of the Joint Annual Meeting ISMRM-ESMRMB*, Berlin, May 19–25, 2007; p. 164.
106. IEC. International standard, medical equipment – part 2: particular requirements for the safety of magnetic resonance equipment for medical diagnosis, 2<sup>nd</sup> revision, 601-2-33. International Electrotechnical Commission, Geneva, 2002.
107. Collins CM, Smith MB. Spatial resolution of numerical models of man and calculated specific absorption rate using the FDTD method: a study at 64 MHz in a magnetic resonance imaging coil. *J. Magn. Reson. Imaging* 2003; 18: 383–388.
108. Collins CM, Liu W, Wang JH, Gruetter R, Vaughan JT, Ugurbil K, Smith MB. Temperature and SAR calculations for a human head within volume and surface coils at 64 and 300 MHz. *J. Magn. Reson. Imaging* 2004; 19: 650–656.
109. Hand JW, Li Y, Thomas EL, Rutherford MA, Hajnal JV. Prediction of specific absorption rate in mother and fetus associated with MRI examinations during pregnancy. *Magn. Reson. Med.* 2006; 55: 883–893.
110. Zhai Z, DeMeester GD, Morich MA, Shvartsman SM, Kleihorst RP. Numerical evaluation of B1-field and SAR for heterogeneous and homogeneous body model. In *Proceedings of the 12<sup>th</sup> Scientific meeting of the International Society for Magnetic Resonance in Medicine*, Kyoto, 2004; p. 666.

111. Nguyen UD, Brown JS, Chang IA, Krycia J, Mirotznik MS. Numerical evaluation of heating of human head due to magnetic resonance image. *IEEE Trans. Biomed. Eng.* 2004; 51: 1301–1309.
112. Hand JW, Lagendijk JJW, Hajnal JV, Lau RW, Young IR. SAR and temperature changes in the leg due to an RF decoupling coil at frequencies between 64 and 213 MHz. *J. Magn. Reson. Imag.* 2000; 12: 68–74.
113. Hand JW, Lau RW, Lagendijk JJW, Ling J, Burl M, Young IR. Electromagnetic and thermal modeling of SAR and temperature fields in tissue due to an RF decoupling coil. *J. Magn. Reson. Imaging* 1999; 42: 183–192.
114. Wu DG, Shamsi S, Chen J, Kainz W. Evaluations of specific absorption rate and temperature increase within pregnant female models in magnetic resonance imaging birdcage coils. *IEEE Trans. Microw. Theory Tech.* 2006; 54: 4472–4478.
115. Nadobny J, Szimtenings M, Diehl D, Stetter E, Brinker G, Wust P. Evaluation of MR-induced hot spots for different temporal SAR modes using a time-dependant finite-difference method with explicit temperature gradient treatment. *IEEE Trans. Biomed. Eng.* 2007; 54: 1837–1850.
116. Mao W, Wang Z, Smith MB, Collins CM. Calculation of SAR for transmit coil arrays. *Concepts in Magnetic Resonance Part B – Magnetic Resonance Engineering* 2007; 31B: 127–131.